1 **Peculiar wave structure of the mesospheric sporadic sodium**

2 **layer observed by lidars in Hefei (31.8N, 117.3E) and Wuhan**

3 **(30.5N, 114E), central China**

4 Mengxi Shi[1], Shican Qiu[1,2*], Willie Soon[3,4], Victor Manuel Velasco Herrera[5], Xianghui Xue[2],

5 Tao Li[2], Xiankang Dou[2*]

6 [1] Department of Geophysics, College of the Geology Engineering and Geomatics, Chang'an

7 University, Xi'an, 710054, China.

8 [2] Key Laboratory of Geospace Environment, Chinese Academy of Sciences, University of

9 Science & Technology of China, Hefei, Anhui, 230026, China.

10 [3] Center for Environmental Research and Earth Sciences (CERES), Salem, MA 01970, USA.

11 [4] Institute of Earth Physics and Space Science (ELKH EPSS), 9400, Sopron, Hungary.

12 [5] Instituto de Geofísica, Universidad Nacional Autónoma De México, Mexico City, Mexico.

13 Corresponding author: Shican Qiu (scq@ustc.edu.cn) and Xiankang Dou (dou@ustc.edu.cn)

14 **Key Points:**

15 • Joint measurements by four lidar beams exhibit a peculiar Na_S with distinguished C-
16 shape and wave structure of large horizontal scale.

17 • The Na_S event corresponds well to the region where the Richardson's stability parameter,
18 *Ri*, is persistently larger than 10, indicating an extremely stable state of the mesopause.

19 • Results from Lomb-Scargle periodogram analysis suggest the occurrence of the Na_S
20 caused by a gravity wave, and its end related to the wave breaking.

21

22 **Abstract**

23 Lidar observations are an effective tracker for identifying atmospheric wave signals. In this

24 research, observations through three lidars are utilized to study the wave structures. A broadband

25 sodium fluorescence lidar and a narrowband Temperature/Wind (T/W) lidar located at Hefei

26 (31.8°N, 117.3°E), while the third lidar system, a broadband lidar system, is located in Wuhan

27 (30.5°N, 114.4°E), about 310 km from Hefei. The three lidars can observe sodium density,

28 temperature and wind profiles simultaneously. Joint sodium density measurements by the fourth

29 lidar beams from Wuhan and Hefei yield a peculiar Na_S with distinguished C-structure and a

30 large horizontal scale of wave structure over more than 310 km, on 21st December, 2014. The

31 Na_S event occurring at 14:20 UT to 17:50 UT corresponds well to the region where the

32 Richardson Number (Ri) is larger than 10, which in turn indicates that the Na_S was formed in an

33 extremely stable atmosphere. Results from the Lomb-Scargle periodogram analysis suggest that

34 the occurrence and evolution of this Na_S event may have been caused by a gravity wave with a

35 period of about 1.25 h, and its end is closely related to the gravity wave fragmentation caused by

36 convective instability.

37 **Key words**: sodium layer, lidar, gravity wave, Lomb-Scargle periodogram analysis

38 **Plain Language Summary**

39 The sporadic sodium layer (SSLs or Na_S) is the most fascinating phenomenon observed from the

40 mesospheric layer. On December 21, 2014, a peculiar Na_S, exhibiting distinguished C-structure

41 and wave characteristics, was observed by four lidar beams, which came from a sodium

42 fluorescence lidar and a temperature and wind (T/W) lidar at Hefei and a sodium fluorescence

43 lidar at Wuhan. The Na_S event corresponds well to the region where the Richardson Number (Ri)

44 is larger than 10, which indicates that this event was formed in an extremely stable atmosphere.

45 Results from the Lomb-Scargle spectral analysis and instability analysis suggest that the

46 occurrence of this Na_S is closely related to the propagation and breaking of gravity waves.

47

1 Introduction

48

49   The sodium layer, which is located between about 80 ~ 110 km, serves an essential role in

50   detecting and quantifying the MLT (mesosphere-lower thermosphere) parameters by means of

51   fluorescence resonance lidars (Gardner et al., 1986; Gong et al., 1997; Liu et al., 2013; Krueger

52   et al., 2015; She et al., 2021). With an active chemical property and high abundance of sodium

53   atoms, the sodium layer has been widely observed and studied all over the world (Plane, 2003;

54   Plane et al., 1998; Plane et al., 1999; Qian et al., 1998). It has also been shown that some regions

55   of the sodium layer at altitudes greater than 85 km can be used as tracers for dynamic

56   disturbances under normal conditions (Gardner and Voelz, 1987; Xu and Smith, 2004; Zhou and

57   Mathews, 1995). Lidar observations provide a reliable means of identifying atmospheric wave

58   signals (Gardner et al., 2019; Gardner and Voelz, 1987; Gong et al., 2015; Li et al., 2007a; Li et

59   al., 2007b).

60   The sporadic sodium layer (SSLs or Na_S), with the neutral sodium density that could be

61   doubled within several minutes, is the unique but most puzzling   phenomenon observed from

62   the sodium layer. The current existing views indicate that Na_S is originated from sporadic E

63   layers (E_S) (Collins et al., 2002; Cox et al., 1993) or triggered by enhancement of temperature

64   (Zhou et al., 1993). Further observations show that Na_S is closely related to wave fluctuations

65   (Clemesha et al., 1997; Kane et al., 1991; Li et al., 2005; Qian et al., 1998; Tsuda et al., 2011;

66   Zhou and Mathews, 1995). Many observational results reveal that Na_S is frequently accompanied

67   with gravity waves (Ban et al., 2015; Li et al., 2007a; Li et al., 2007b; Qian et al., 1998).

68   Meanwhile, the fine structures of Na_S manifest distinct characters related to waves on short time

69   scale (Chen and Yi, 2011; Liu and Yi, 2009; Liu et al., 2013). The bursts of the sodium atoms

70   show a pulse period of 30 seconds (Liu and Yi, 2009), indicating some kind of small-scale

71   atmospheric perturbation effects on the evolution of Na_S (Liu and Yi, 2009; Sarkhel et al., 2019).

72   In this research, observations from three lidars are utilized to study the wave structures from

73   the mesospheric sodium layer. A sodium fluorescence lidar (Dou et al., 2009) and

74   Temperature/Wind (T/W) lidar (Li et al., 2012) located at Hefei (31.8°N, 117.3°E), while

75   another sodium fluorescence lidar located at Wuhan (30.5°N, 114.4°E) 310 km away from Hefei.

76   We obtained sodium density profiles using the sodium fluorescence lidars and the T/W lidar, and

77   temperature and wind field profiles using the T/W lidar. A peculiar Na_S, exhibiting distinguished

78   C-structure and wave characteristics, was observed by fourth, combined signals of Hefei and

79   Wuhan, lidar beams on 21st December, 2014.

80   **2 Observations and Results**

81   The sodium fluorescence lidar of the University of Science and Technology of China

82   (USTC) located at Hefei with one lidar beam that can detect the fine structures of sodium layer.

83   The narrowband T/W lidar, located nearby, measures and diagnoses   the sodium density,

84   temperature and wind with two beams. The Wuhan University sodium fluorescence lidar located

85   about 350 km from Hefei, with one lidar beam observing the sodium density. The locations for

86   the four beams of the three lidars are shown in Figure 1. In this study, we select candidate Na_S

87   events using the criteria proposed by Dou et al., which stipulates that the maximum density of

88   the Na_S peak must be at least two times higher than that of the background sodium layer at the

89   same altitude and must be more than $1000\ cm^{-3}$ if the altitude of a Na_S event was higher than

90   100 km (Dou et al., 2009). The data processing program set quality control standards for the

91   temperature and zonal wind data from the T/W lidar, namely: 1. the temperature data should be

92   greater than 100 K and less than 300 K, and the error value should be less than 20 K; 2. the

93   absolute value of the zonal wind speed should be less than 200 m/s, and the error value should be

94   less than 40 m/s. Since the meridional wind data observed by the T/W lidar are not available, we

95   supplemented the data analysis with data observed by the meteor lidar located in Wuhan.

96   On December 21, 2014, a peculiar structure of Na_S was detected by the three lidars over

97   Hefei and Wuhan, respectively. Figure 2a to 2d show the sodium density profiles from the total

98   of four lidar beams. The Na_S is located near 100 km, much higher than the main sodium layer,

99   which usually has a centroid at 92 km. The Na_S was maintained at about 101 kilometers at 14:20

100   UT and dropped to about 97 km at 17:50 UT, with a decline rate of about 1.14 km per hour and

101   an obvious C-shaped structure. The Na_S occurred almost at the same time according to the four

102   lidar beams, indicating a large horizontal scale of wave structure over more than 310 km.

103   Figure 3 indicates the temperature profile and zonal wind distribution from the T/W lidar

104   throughout the night. It demonstrates that the Na_S occurred during an extremely cold phase of

105   mesopause temperature, which remained below 180 K at around 100 km altitude from 12:00 UT

106   to 16:00 UT (Figure 3a). On the other hand, the zonal wind switched from west phase to east

107   phase between 14:00 UT and 15:00 UT near 100 km (Figure 3b). This windshear is in accord

108   with the generation of E$_S$, with a westward wind below and an eastward wind above (Hines,

109   1964). However, there is no temporal correlation between this Na$_S$ event (which occurred at

110   14:20 UT) and the E$_S$ detected in Wuhan at 08:15 UT.

111   **3 Discussions**

112   Dynamic stability can be characterized by the Richardson number, *Ri*, which is defined as

113
$$Ri = \frac{N^2}{S^2},$$
(1)

114   where *N* is the buoyancy frequency, which reflects the degree of the atmospheric convective

115   stability. *N* is defined as

116
$$N^2 = \frac{g}{T}\left(\frac{\partial T}{\partial z} + \frac{g}{C_p}\right),$$
(2)

117   where *g* is the gravitational acceleration with a value of 9.5 ms^{-2} in the mesopause region, *T* is

118   the atmospheric temperature, and C_p is the specific heat at constant pressure with a value of

119   1004 $J\ K^{-1}\ kg^{-1}$. And *S* represents the total vertical wind shear

120
$$S^2 = \left(\frac{\partial u}{\partial z}\right)^2 + \left(\frac{\partial v}{\partial z}\right)^2,$$
(3)

121   where *u* and *v* are the zonal and meridional wind velocities, respectively (Nappo, 2012).

122   *Ri* represents the ratio of the production or suppression of turbulence kinetic energy by

123   buoyant forces (N^2) relative to the mechanical production of turbulence kinetic energy by shear

124   forces (S^2) (Nappo, 2012). $Ri > 0.25$ is considered a sufficient condition for dynamic

125   stability, where the fluid will return to its initial state if disturbed by a small vertical

126   displacement (Nappo, 2012). Dynamic instability would occur over the range $0 \leq Ri \leq 0.25$,

127   and the condition for convective instability is $Ri < 0$ (or $N^2 < 0$) (Nappo, 2012).

128   The vertical interval for both temperature and wind velocity from the USTC T/W lidar east beam

129   and west beam is 0.5 km, so the expression for Ri at a given altitude of z_0 could be written as

130
$$Ri_{z_0} = \frac{N_{z_0}^2}{S_{z_0}^2} = \frac{\frac{g}{T}\left(\frac{\partial T}{\partial z} + \frac{g}{C_p}\right)}{\left(\frac{\partial u}{\partial z}\right)^2 + \left(\frac{\partial v}{\partial z}\right)^2} \approx \frac{\frac{g}{T_0}\left(\frac{T_{z_0+0.5}-T_{z_0-0.5}}{\Delta h} + \frac{g}{C_p}\right)}{\left(\frac{u_{z_0+0.5}-u_{z_0-0.5}}{\Delta h}\right)^2 + \left(\frac{v_{z_0+0.5}-v_{z_0-0.5}}{\Delta h}\right)^2}$$
$$= \frac{\frac{9.5}{1000}\cdot\frac{T_{z_0+0.5}-T_{z_0-0.5}}{T_{z_0}} + \frac{9.5^2}{1004}\cdot\frac{1}{T_{z_0}}}{\left((u_{z_0+0.5}-u_{z_0-0.5})^2 + (v_{z_0+0.5}-v_{z_0-0.5})^2\right)\times 10^{-6}},$$
(4)

131   where $\Delta h = (z_0 + 0.5) - (z_0 - 0.5) = 1km = 1000m$.

132   Because meridional wind data observed by temperature/wind lidar are not available, we

133   have used the meridional wind data observed by the meteor lidar located in Wuhan as a

134   supplement/substitute (as shown in Figure 3c) to derive and quantify the Ri values, as Ban et al.

135   have done (Ban et al., 2015).

136   From 14:00 UT to 18:00 UT, a temperature inversion layer appears on the temperature

137   profile (Figure 3a) at altitudes between 105 km and 96 km (above the extremely cold region).

138   Due to the presence of the temperature inversion layer, the stability of the atmosphere medium

139   above and below it was weakened by the large temperature gradient, resulting in some unstable

140   zones. The rapid change in temperature is consistent with possible wave breaking similar to that

141   observed by Li et al. (2007b). To explore this possibility of gravity waves breaking, the

142   buoyancy frequency square N^2 and the Richardson number Ri are shown in Figure 4a and

143   Figure 4b, respectively. As indicated by Figure 4a, an N^2 enhancement layer ($N^2 > 9$) dropped

144   from 102 km at 14:00 UT to around 99 km at 16:00 UT. There was also a significant unstable

145   zone ($N^2 < 0$), which was located near 100 km, corresponding to the time periods of 17:35–

146   18:10 UT. Figure 4b depicts the Ri profiles at 99 km and 99.5 km between 17:30 UT and 18:30

147   UT. The variation of Ri values illustrates that the mesopause region has undergone drastic

148   stability changes during this brief one-hour interval. Another thing to note is that most of these

149   Ri values are less than 0 and the zonal wind field is not strongly disturbed (less than $10m/s/km$

150   as shown in Figure 3b) from 17:40 UT to 18:15 UT. This observation suggests that the presence

151   of the aforementioned temperature inversion layer has caused the convective instability of the

152   mesopause during this period and may be the cause for the breaking of gravity waves.

153   Furthermore, because Ri and N^2 are calculated from the temperature profile obtained by

154   smoothing the 15-point time series data (with a time window length of approximately 24

155   minutes) and have a spatial resolution of only 0.5 km, structures that existed for only a short

156   period of time or over a very restricted vertical region may not be fully resolved or captured.

157   Therefore, we believe that convective instability was probably responsible for the sharp fall

158   of Ri and N^2 values in the mesopause, but it cannot be completely ruled out if small-scale

159   dynamic instability also contributed to the process in some ways.

160   Figure 5 indicates the distribution of Ri values at 6 min temporal resolution and 0.5 km

161   spatial resolution superimposed on the sodium density contour plot. As can be seen in Figure 5a,

162   the Na$_S$ event occurred between 14:20 UT and 17:50 UT corresponds well to the Ri stable point

163    $(Ri > 10)$ region, which indicates that this Na$_S$ event was formed in an extremely stable state of

164   the mesopause. Figure 5b shows that from about 17:40 UT to 18:15 UT, the atmosphere at 98.5-

165   100 km underwent a strong unstable process/condition (within this region, Ri is less than 0).

166   Combined with the information obtained from Figure 4b, this instability event and process is

167   most likely caused by the convective instability triggered by the presence of the temperature

168   inversion layer in the mesopause. On the other hand, the peak sodium density gradually dropped

169   and returned to the usual sodium density distribution at 97 km around 17:50 UT, which

170   corresponds well to the spatiotemporal distribution of the Ri unstable point regions in Figure 5b.

171   Overall, the whole course of this Nas event is closely related to the Ri values controlled by

172   horizontal wind and temperature, implying that gravity wave modulations played an important

173   role.

174   In order to explore the role of fluctuations in this Na$_S$ event, a power spectrum analysis of

175   the data is necessary. The lidar-generated observations in Hefei and Wuhan are not always

176   continuous and have various breakpoints and data gaps. In this study, the power spectrum of

177   such non-uniformly distributed data with observational breakpoints/data gaps was calculated

178   using the Lomb-Scargle spectral analysis method.

179   This spectral analysis approach is also known as the "Lomb-Scargle periodogram method,"

180   since N. Lomb devised a method (Lomb, 1976) for power spectrum analysis of non-uniformly

181   sampled data and J. Scargle further optimized the method (Scargle, 1982). The advantage of

182   Lomb-Scargle spectrum analysis is that it can yield a high-resolution spectrum (resolution higher

183   than 1/T, where T is the time span), which can more precisely pinpoint the location of the

184   spectrum peaks. It also avoids the need for data interpolation. Here is a quick explanation of this

185   method.

186   Suppose the data set h_i with *N* points is as follows (Lomb, 1976; Scargle, 1982):

187
$$h_i = h(t_i), i = 1,2, \dots, N. \tag{5}$$

188   The mean value of the data set h_i with *N* points is:

189
$$\overline{h} = \frac{1}{N} \Sigma_1^N h_i,$$
(6)

190   the variance of the data set is:

191
$$\sigma^2 = \frac{1}{N-1} \sum_1^N (h_i - \overline{h})^2,$$
(7)

192   then the Lomb-normalized periodogram is defined as (Lomb, 1976; Scargle, 1982):

193
$$P_N(\omega) = \frac{1}{2\sigma^2} \left[\frac{\left(\sum_i (h_i - \overline{h}) \cos \omega(t_i - \tau) \right)^2}{\sum_i \cos^2 \omega(t_i - \tau)} + \frac{\left(\sum_i (h_i - \overline{h}) \sin \omega(t_i - \tau) \right)^2}{\sum_i \sin^2 \omega(t_i - \tau)} \right],$$
(8)

194   where τ is the time constant given by the following relation:

195
$$\tan(2\omega\tau) = \frac{\sum_i \sin 2\omega t_i}{\sum_i \cos 2\omega t_i},$$
(9)

196   The time constant τ can be chosen so that $P_N(\omega)$ does not change owing to any constant
197   translation of the t sequence, and Eq. (8) is identical to the least-squares harmonic fit shown
198   below:

199
$$h(t) = A\cos \omega t + B \sin \omega t,$$
(10)

200   The advantages of the Lomb-Scargle spectrum analysis method over the FFT method are
201   demonstrated by Eq. (8) and Eq. (10). In order to fully utilize the data present in the dense points,
202   Eq. (8) calculates the spectral intensity based on "point" weighting as opposed to "equal time
203   interval" weighting. Contrarily, using the "equal time interval" (FFT method) approach to cope
204   with unevenly sampled data may result in significant spectral leakages and false determination of
205   periodicities.

206   The contour plot of the Lomb-Scargle power spectrum based on the day's observations (the
207   90% significant level is plotted with a white solid contour line in Figure 6a) and the zonal wind
208   profile at 100.5 km (Figure 6b) are shown in Figure 6. At 100.5 km, the zonal wind began to
209   speed up eastward at 13:40 UT, and there were fluctuations with a period of 1.3 hours and an
210   amplitude of around 35 m/s between 14:10 UT and 18:05 UT, as depicted in Figure 6b. The
211   Lomb-Scargle power spectrum (Figure 6a) also had a similar periodic feature (as shown by
212   Figure 6a, the power of wave with 1.25-hour period is strong with above the 90% confidence
213   level at 100.5 km). After 18: 05 UT, the zonal wind abruptly decreased as the 1.3-hour wave
214   oscillation disappeared because of the breaking of gravity wave between 17:40 UT to 18:15 UT.

215   As a result, the rising temperature, occurrence of this Na$_S$ event and zonal wind field shear

216   between 14:10 UT and 18:05 UT around 100 km are most possibly generated by a gravity wave

217   with an apparent period of 1.3 hours. The absence of waves in the zonal wind field before 14:10

218   UT and after 18:05 UT further supports this assertion.

219   **4 Conclusion**

220   On December 21, 2014, between 14:00 and 16:00 UT, the Wuhan and Hefei sodium lidar

221   systems detected a strong zonal wind shear approaching around 100 km height. At the same

222   time, this region has an extremely low temperature and a significant temperature gradient from

223   its surroundings. Joint sodium density measurements from Wuhan and Hefei indicate the

224   formation of a Na$_S$ event with a horizontal scale of more than 310 km occurred between 14:20

225   and 17:50 UT.

226   Between 14:10 and 18:05 UT, the zonal wind field profile at 100.5 km indicates a

227   noticeable fluctuation characteristic with an apparent period of 1.3 hours. This coincides with the

228   fluctuations over a 1.25-hour period calculated by the Lomb-Scargle power spectrum at 100.5

229   km. Both the high stability of the mesopause during this time period and fluctuations with a 1.25-

230   hour period around 100 km indicated by the Lomb-Scargle power spectrum suggest the existence

231   of gravity waves. The instability analysis' findings reveal that between 17:30 and 18:30 UT, the

232   atmosphere at 99.5-100 km altitude exhibits significant stability changes over time. It is

233   noteworthy that the presence of a convective instability layer from 17:40 UT to 18:15 UT

234   provided favorable conditions for the breaking of gravity waves during this time and ended this

235   Na$_S$ event at about 17:50 UT.

236   In conclusion, the occurrence and evolution of this Na$_S$ event may have been caused by a

237   gravity wave with a period of about 1.25 h, and its termination related to the gravity wave

238   breaking caused by convective instability.

239   **Open Research**

240   Observations of wind field, temperature and sodium density detected by Temperature/Wind

241   (T/W) lidar in Hefei are available from the University of Science and Technology of China.

242   Atmospheric temperature in the MLT region of sodium temperature and wind lidar over Hefei.

243   V1.0. National Space Science Data Center. (DOI:10.12176/01.05.027. 2011-11-20). The

244 observations of sodium density detected by sodium fluorescence lidars in Hefei and Wuhan are

245 available from University of Science and Technology of China. Photon counting data of

246 Fluorescence scattering of LIDAR at USTC Station, Hefei. V1.0. National Space Science Data

247 Center. (DOI:10.12176/01.05.056. 2010-08-09), Wuhan University. Photon counting data of

248 Fluorescence scattering of LIDAR at Luojia Hill Station, Wuhan. V1.0. National Space Science

249 Data Center. (DOI:10.12176/01.05.063. 2010-05-25), respectively.   The observations of

250 meridional wind detected by meteor lidar in Wuhan are available from University of Science and

251 Technology of China. Meteor observation data from meteor radar at Zuoling station, Wuhan.

252 V1.0. National Space Science Data Center. (DOI:10.12176/01.05.004. 2020-02-27).

258 **References**

259 Ban, C., T. Li, X. Fang, X. K. Dou, and J. G. Xiong (2015), Sodium lidar-observed gravity wave
260   breaking followed by an upward propagation of sporadic sodium layer over Hefei, China,
261   *Journal of Geophysical Research: Space Physics, 120,* doi:10.1002/2015JA021339.

262 Chen, L., and F. Yi (2011), Average properties and small-scale variations of the mesospheric Na
263   and Fe layers as observed simultaneously by two closely colocated lidars at 30° N, *Annales*
264   *Geophysicae, 29*, 1037-1048.

265 Clemesha, B. R., P. P. Batista, and D. M. Simonich (1997), Wave-Associated Sporadic Neutral
266   Layers in the Upper Atmosphere, paper presented at 5th International Congress of the
267   Brazilian Geophysical Society, doi:10.1590/S0102-261X1997000300003.

268 Collins, S. C., J. M. C. Plane, M. C. Kelleya, T. G. Wright, P. Soldán, T. J. Kanee, A. J. Gerrard,
269   B. W. Grime, R. J. Rollason, J. S. Friedman, S. A. Gonzàlez, Q. Zhou, M. P. Sulzer, C. A.
270   Tepley (2002), A study of the role of ion-molecule chemistry in the formation of sporadic
271   sodium layers, *Journal of Atmospheric and Solar-Terrestrial Physics*, *64*, 845-860.

272 Cox, R. M., J. M. C. Plane, and J. S. A. Green (1993), A modelling investigation of sudden sodium
273   layers, *Geophysical Research Letters*, *20*(24), 2841-2844.

274 Dou, X. K., X. H. Xue, T. D. Chen, W. X. Wan, T. Li, C. Chen, S. Qiu, and Z. Y. Chen (2009), A
275   statistical study of sporadic sodium layer observed by Sodium lidar at Hefei (31.8° N, 117.3°
276   E), *Annales Geophysicae*, *27*, 2247-2257.

277 Gardner, C. S., Y. F. Guo, and A. Z. Liu (2019), Parameterizing Wave-Driven Vertical Constituent
278   Transport in the Upper Atmosphere, *Earth and Space Science*, *6*, 904-913.

279 Gardner, C. S., and D. G. Voelz (1987), Lidar studies of the nighttime sodium layer over Urbana,
280   Illinois: 2. Gravity waves, *Journal of Geophysical Research: Space Physics*, *92*(A5), 4673-

281   4694.

282 Gardner, C. S., D. G. Voelz, C. R. Philbrick, and D. P. Sipler (1986), Simultaneous lidar
283   measurements of the sodium layer at the Air Force Geophysics Laboratory and the University
284   of Illinois, *Journal of Geophysical Research: Space Physics*, *91*(A11), 12131-12136.

285 Gong, S. H., G. T. Yang, X. W. Cheng, S. S. Gong, J. Y. Xu, F. Q. Li, W. Gong, and J. H. Wang
286   (2015), Lidar observation campaigns on diurnal variations of the sodium layer in Beijing and
287   Wuhan, China, *Science China Earth Sciences*, *58*(8), 1377-1386.

288 Gong, S. S., X. Z. Zeng, X. Xue, W. G. Zheng, Z. L. Hu, H. C. Jia, H. Z. Zhang, and Y. P. Liu
289   (1997), First time observation of sodium layer over Wuhan, China by sodium fluorescence
290   lidar, *Science in China Series A*, *40*(11), 1228-1232.

291 Hines, C. O. (1964), The formation of midlatitude sporadic E layers, *Journal of Geophysical
292   Research*, *69*(5), 1018-1019.

293 Kane, T. J., C. A. Hostetler, and C. S. Gardner (1991), Horizontal and vertical structure of the
294   major sporadic sodium layer events observed during ALOHA-90, *Geophysical Research
295   Letters*, *18*(7), 1365-1368.

296 Krueger, D. A., C.-Y. She and T. Yuan (2015), Retrieving mesopause temperature and line-of-sight
297   wind from full-diurnal-cycle Na lidar observations, *Applied Optics, 54*(32), 9469-9489.

298 Li, F., A. Z. Liu, G. R. Swenson, J. H. Hecht, and W. A. Robinson (2005), Observations of gravity
299   wave breakdown into ripples associated with dynamical instabilities, *Journal of Geophysical
300   Research: Atmospheres*, *110*, D09S11, doi:10.1029/2004JD004849.

301 Li, T., X. Fang, W. Liu, S. Y. Gu, and X. K. Dou (2012), Narrowband sodium lidar for the
302   measurements of mesopause region temperature and wind, *Applied Optics*, *51*(22), 5401-
303   5411.

304 Li, T., C. Y. She, H. L. Liu, T. Leblanc, and I. S. Mcdermid (2007a), Sodium lidar–observed strong
305   inertia-gravity wave activities in the mesopause region over Fort Collins, Colorado (41°N,
306   105°W), *Journal of Geophysical Research: Atmospheres*, *112*, D22104.

307 Li, T., C. Y. She, H. L. Liu, and M. T. Montgomery (2007b), Evidence of a gravity wave breaking
308   event and the estimation of the wave characteristics from sodium lidar observation over Fort
309   Collins, CO (41°N, 105°W), *Geophysical Research Letters*, *34*, L05815.

310 Liu, Y. J, and F. Yi (2009), Behavior of sporadic Na layers on small time scale, *Journal of
311   Atmospheric and Solar-Terrestrial Physics*, *71*(12), 1374-1382.

312 Liu, Y. J., B. R. Clemesha, J. H. Wang, and X. W. Cheng (2013), Comparison of sporadic sodium
313   layer characteristics observed at different time resolutions, *Annales Geophysicae*, *31*(11),
314   1899-1912, doi:10.5194/angeo-31-1899-2013.

315 Lomb, N. R. (1976), Least-squares frequency analysis of unequally spaced data, *Astrophysics and
316   Space Science*, *39*, 447–462, doi:10.1007/BF00648343.

317 Nappo, C. (2012), An introduction to atmospheric gravity waves, International Geophysics, 85, 1–
318   216, 10.1016/b978–0–12–385223–6.00001–x.

319 Plane, J. M. C. (2003), Atmospheric chemistry of meteoric metals, *Chemical Reviews*, *103*(12),
320   4963-4984.

321 Plane, J. M. C., R. M. Cox, J. Qian, W. M. Pfenninger, G. C. Papen, C. S. Gardner, and P. J. Espy
322   (1998), Mesospheric Na layer at extreme high latitudes in summer, *Journal of Geophysical
323   Research: Atmospheres*, *103*(D6), 6381-6389.

324 Plane, J. M. C., R. M. Cox, and R. J. Rollason (1999), Metallic layers in the mesopause and lower
325   thermosphere region, *Advances in Space Research*, *24*(11), 1559-1570.

326 Qian, J., Y. Y. Gu, and C. S. Gardner (1998), Characteristics of the sporadic Na layers observed

during the Airborne Lidar and Observations of Hawaiian Airglow/Airborne Noctilucent Cloud (ALOHA/ANLC-93) campaigns, *Journal of Geophysical Research: Atmospheres*, *103*(D6), 6333-6347.

Sarkhel, S., S. Mondal1, J. Agarwal, D. Chakrabarty, R Sekar, T. Yuan, X. Cai, A. Z. Liu, S. Nozawa, N. Saito, T. D. Kawahara, M. G. Mlynczak and J. M. Russell III (2019): On the long-lasting "C-type" structures in the sodium lidargram: The life-time of Kelvin-Helmholtz billows in the mesosphere and lower thermosphere region, *J. Geophys. Res. Space Physics* 124. https://doi.org/10.1029/2019JA026630.

Scargle, J. D. (1982), Studies in astronomical time series analysis. II-Statistical aspects of spectral analysis of unevenly spaced data, *The Astrophysical Journal*, *263*, 835-853.

She, C.-Y., Liu, A. Z., Yuan, T., Yue, J., Li, T., Ban, C. and Friedman, J. S. (2021). MLT Science Enabled by Atmospheric Lidars. In Upper Atmosphere Dynamics and Energetics (eds W. Wang, Y. Zhang and L.J. Paxton). https://doi.org/10.1002/9781119815631.ch20.

Tsuda, T. T., S. Nozawa, T. D. Kawahara, T. Kawabata, N. Saito, S. Wada, C. M. Hall, S. Oyama, Y. Ogawa, S. Suzuki T. Ogawa, T. Takahashi, H. Fujiwara, R. Fujii,1 N. Matuura, and A. Brekke (2011), Fine structure of sporadic sodium layer observed with a sodium lidar at TromsØ, Norway, *Geophysical Research Letters*, *38*, L18102.

Xu, J. Y., and A. K. Smith (2004), Studies of gravity wave-induced fluctuations of the sodium layer using linear and nonlinear models, *Journal of Geophysical Research: Atmospheres*, *109*, D02306.

Zhou, Q. H., and J. D. Mathews (1995), Generation of sporadic sodium layers via turbulent heating of the atmosphere?, *Journal of Atmospheric and Terrestrial Physics*, *57*(11), 1309-1315.

Zhou, Q. H., J. D. Mathews, and C. A. Tepley (1993), A proposed temperature dependent mechanism for the formation of sporadic sodium layers, *Journal of Atmospheric and Terrestrial Physics*, *55*(3), 513-521.
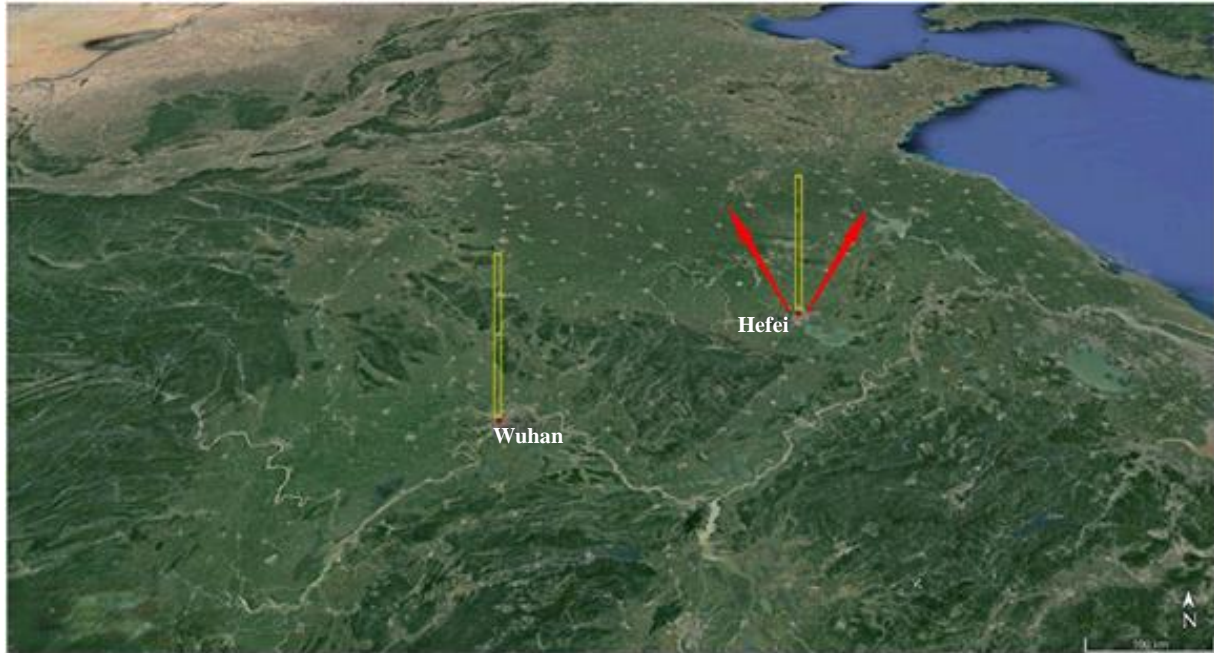
353

354 **Figure 1.** The illustration of the locations of the four lidar beams. The sodium fluorescence lidar

355 of USTC located at Hefei (31.8°N, 117.3°E) with one lidar beam (as shown by the yellow bar

356 near the character 'Hefei'). The narrowband T/W lidar, located nearby, measures the sodium

357 density, temperature and wind through two beams (as shown by the two red arrows) which point

358 east and west at 15° to the zenith, respectively. The sodium fluorescence lidar which located at

359 Wuhan (30.5°N, 114.4°E), whose beam is shown by the yellow bar near the character 'Wuhan'.

360
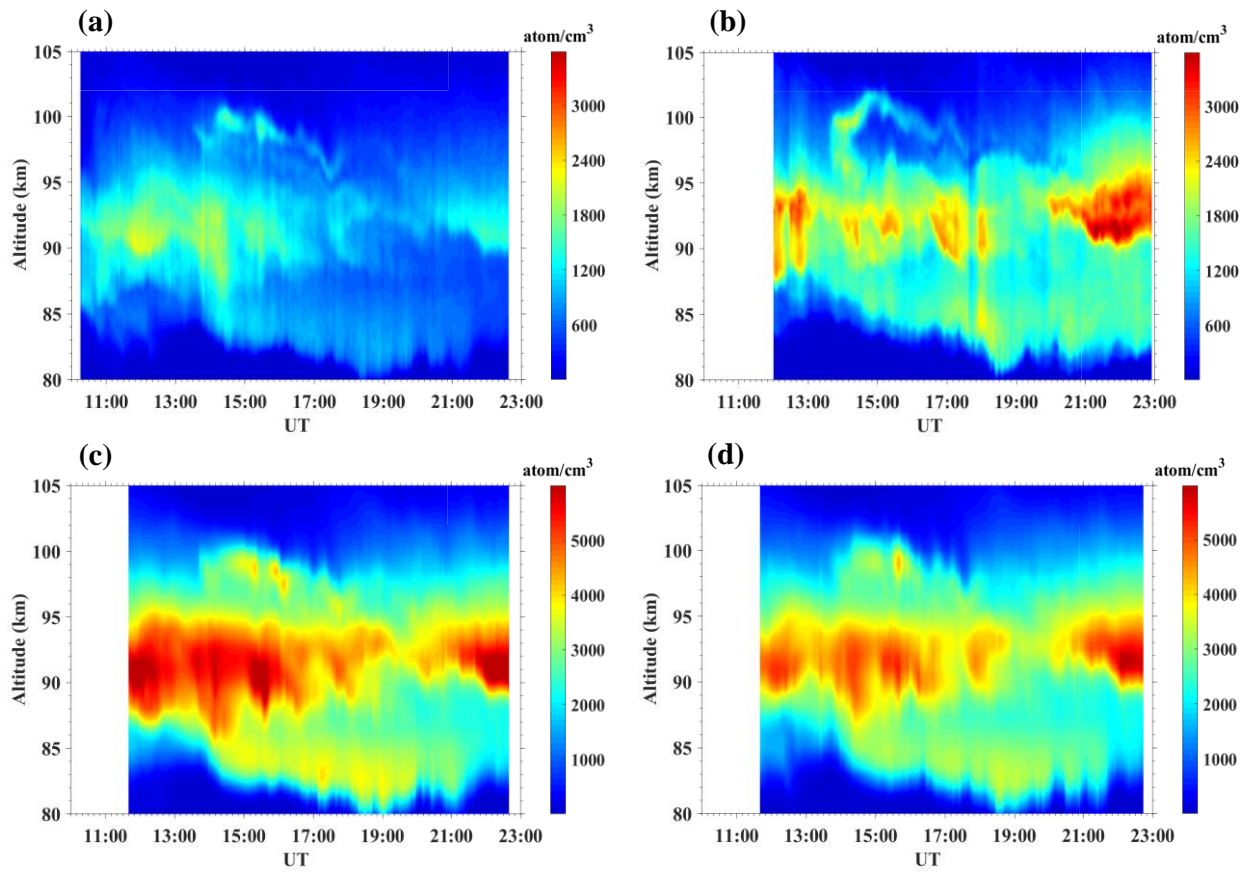
Figure 2. The sodium density profiles on December 21st, 2014, detected by (a) the beam of the USTC sodium fluorescence lidar, which is located in Hefei. (b) the beam of the Wuhan University sodium fluorescence lidar, which is located in Wuhan. (c) the east beam of the USTC narrowband T/W lidar, which is located in Hefei. (d) the west beam of the USTC narrowband T/W lidar.
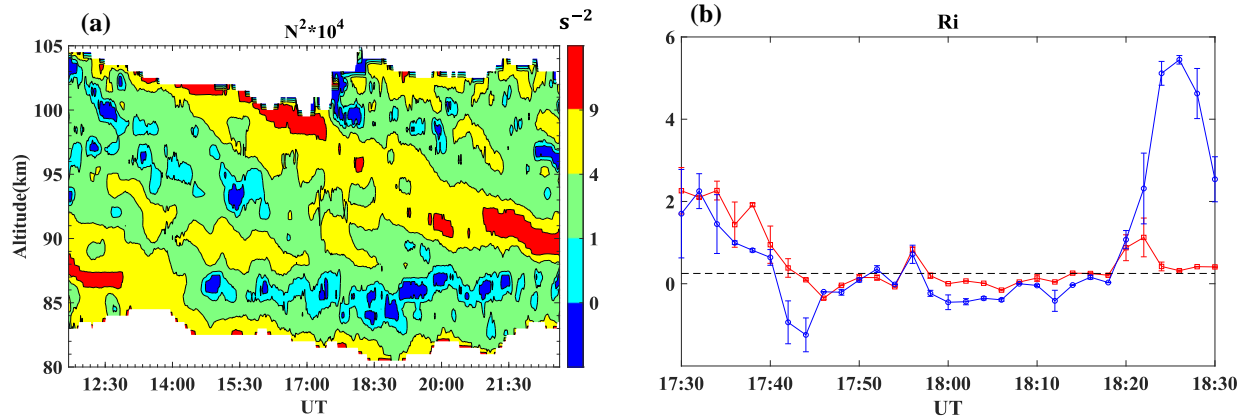
368
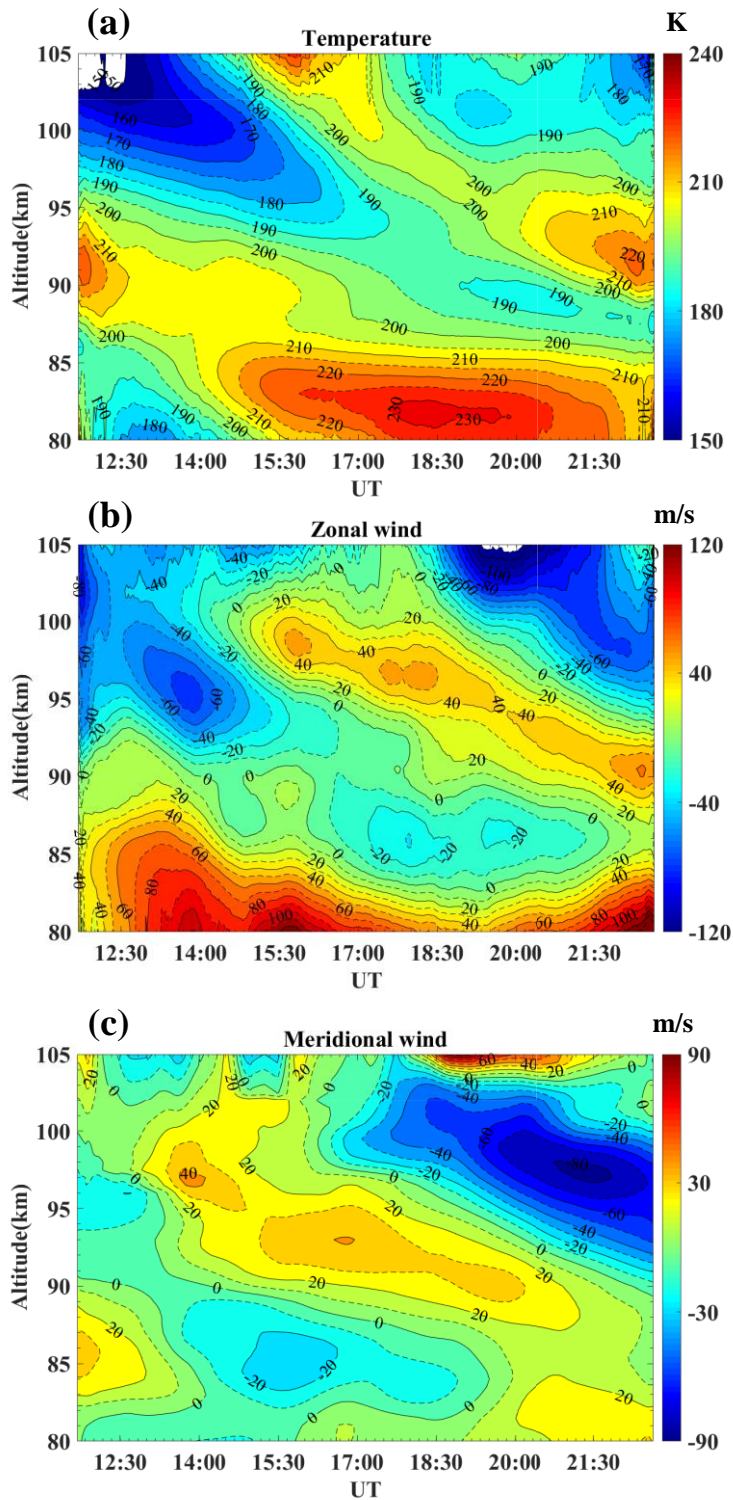
Figure 3. Temperature profile (a) and zonal wind distribution (b), from the USTC T/W lidar. (c)

370   The meridional wind distribution detected by the Wuhan Meteor lidar.
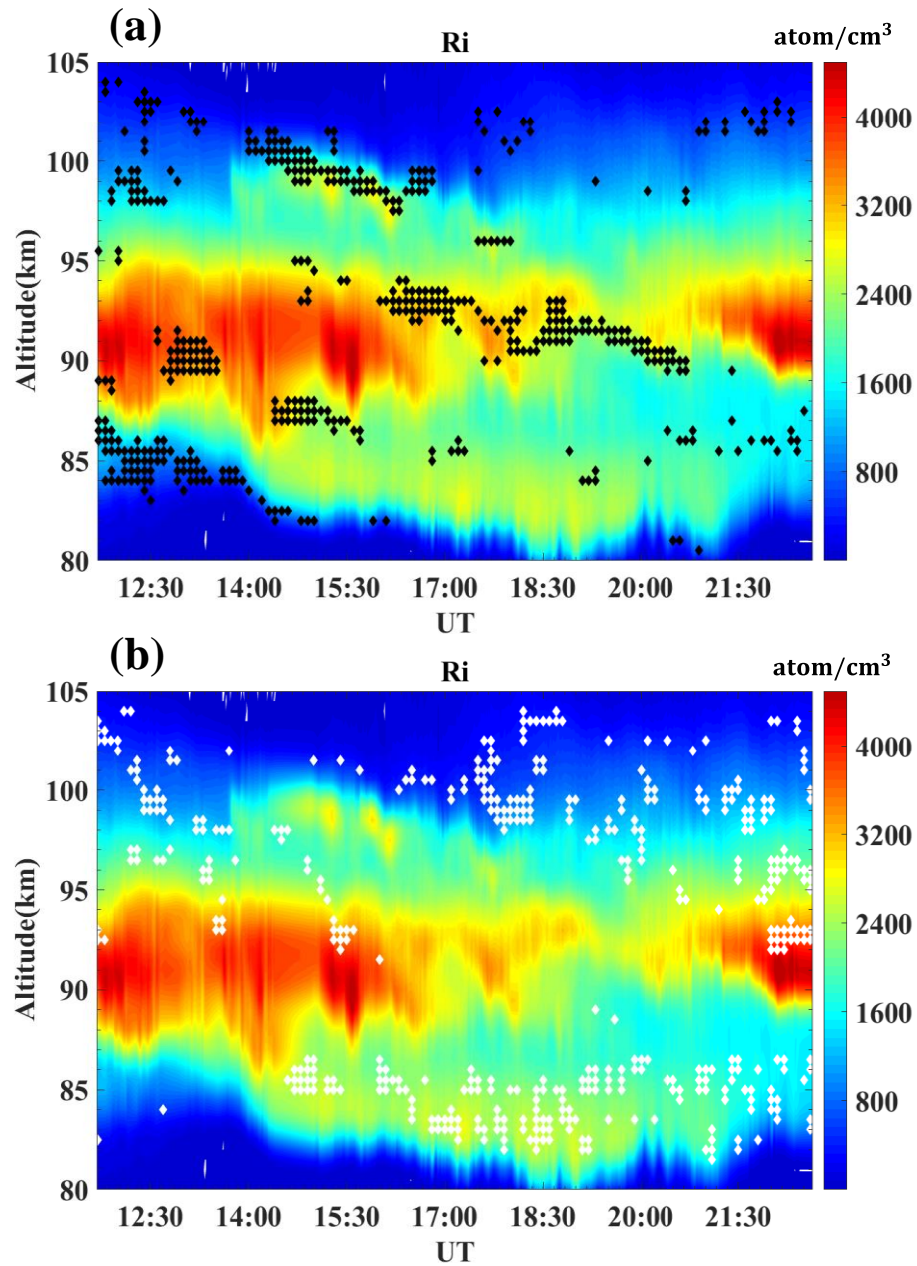
371

372

373 **Figure 4.** (a) The time-height contour plot of Brunt-Vaisala frequency squared (N^2). (b) the

374 Richardson number (Ri) and its error bar between 17:30 UT and 18:30 UT, calculated from

375 temperature, zonal wind data from T/W lidar, and meridional wind data from meteor lidar. Red

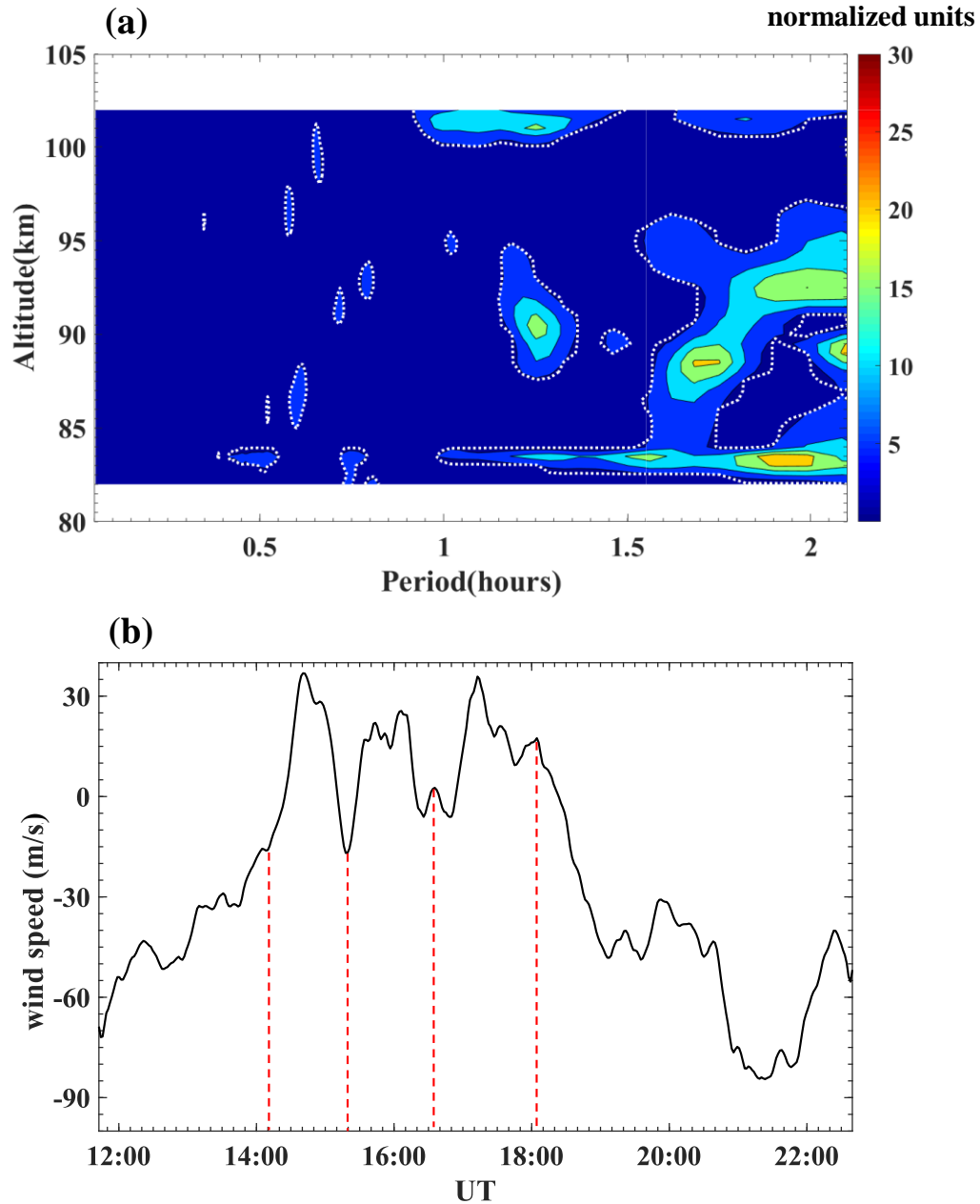376 and blue represent the profiles on 99 km and 99.5 km, respectively.

377

378

Figure 5. (a) *Ri* stable (*Ri* > 10) points (black dots) superimposed on the sodium density contour

plot. (b) *Ri* unstable (*Ri* < 0) points (white dots) superimposed on the sodium density contour

plot.

382

Figure 6. (a) Contour plot of the Lomb-Scargle power spectrum for the zonal wind field on December 21, 2014. (b) The zonal wind field profile at 100.5 km (using 10-point smoothed data). The red dashed line indicates the possible period boundaries of gravity wave.